nature biomedical engineering

Article

https://doi.org/10.1038/s41551-023-01148-5

Photoacoustic vector tomography for deep haemodynamic imaging

Received: 15 August 2022

Accepted: 25 October 2023

Published online: 30 November 2023

Check for updates

Yang Zhang[1,3], Joshua Olick-Gibson[1,3], Anjul Khadria[1] & Lihong V. Wang[1,2]

Imaging deep haemodynamics non-invasively remains a quest. Although optical imaging techniques can be used to measure blood flow, they are generally limited to imaging within ~1 mm below the skin's surface. Here we show that such optical diffusion limit can be broken through by leveraging the spatial heterogeneity of blood and its photoacoustic contrast. Specifically, successive single-shot wide-field photoacoustic images of blood vessels can be used to visualize the frame-to-frame propagation of blood and to estimate blood flow speed and direction pixel-wise. The method, which we named photoacoustic vector tomography (PAVT), allows for the quantification of haemodynamics in veins more than 5 mm deep, as we show for regions in the hands and arms of healthy volunteers. PAVT may offer advantages for the diagnosis and monitoring of vascular diseases and for the mapping of the function of the circulatory system.

In vivo haemodynamic imaging provides invaluable functional information in tissues and organs. Biomedical optical imaging techniques, such as Doppler-based methods[1] (laser Doppler flowmetry[2], Doppler optical coherence tomography[3]), speckle-based methods[4] (laser speckle contrast imaging[5]) and red-blood-cell-tracking methods (confocal microscopy[6]) can map the dynamics of blood flow owing to the intrinsic optical contrast of blood. However, these techniques suffer from shallow depth penetration because of strong ballistic light attenuation in biological tissue. Thus, imaging blood flow with fine spatial resolution at depths beyond the optical diffusion limit (>1 mm)[7] by pure optical imaging remains challenging. Unlike pure optical imaging modalities, photoacoustic tomography (PAT) combines optical absorption contrast with low scattering ultrasonic detection to enable high spatiotemporal resolution and deep tissue imaging of endogenous chromophores, such as haemoglobin[8]. As such, PAT is uniquely positioned as a functional, anatomical and molecular modality that can image blood vessels beyond the optical diffusion limit with fine spatial resolution[7].

PAT primarily has three main forms of implementation: optical resolution photoacoustic microscopy (OR-PAM), acoustic resolution photoacoustic microscopy (AR-PAM) and photoacoustic computed tomography (PACT) (ref. 7). All three techniques have excellent optical contrast for imaging blood vessels, yet only OR-PAM has been shown to measure blood flow in vivo[9]. OR-PAM uses point-by-point scanning of an optical focus to enable transverse spatial resolution on the order of micrometres[7]. As such, OR-PAM can measure blood flow by tracking individual red blood cells (RBCs) whose diameters range from 7–8 μm[10]. However, this measurement is limited to the optical diffusion limit in biological tissue because of the inability to focus light beyond one transport mean free path[11]. AR-PAM employs raster scanning of an acoustic focus for three-dimensional (3D) imaging at acoustic resolution[11]. Because the resolution in AR-PAM is sacrificed to image deeper than OR-PAM, deep blood flow measurement is challenging because individual RBCs cannot be resolved. Similar in principle to AR-PAM, acoustic resolution photoacoustic doppler flowmetry (AR-PAF) uses wide-field illumination and a single-element focused transducer to calculate A-line cross-correlations between photoacoustic (PA) waveforms. Previous work has demonstrated that ex vivo whole-blood velocity measurement is possible for high centre frequency (f_c) transducers ($f_c \geq 30$ MHz) using AR-PAF (ref. 12), but in vivo blood flow measurement beyond the optical diffusion limit remains an outstanding hurdle. Conversely, PACT uses wide-field illumination coupled with an array of ultrasonic detectors to image vasculature at depths beyond the optical diffusion limit with acoustic resolution[13]. Generally speaking, measuring blood flow in deep tissue with PACT is challenging because (1) compared with OR-PAM, PACT has a lower resolution, preventing it from being able to resolve individual RBCs; (2) the photoacoustic

[1]Caltech Optical Imaging Laboratory, Andrew and Peggy Cherng Department of Medical Engineering, California Institute of Technology, Pasadena, CA, USA. [2]Caltech Optical Imaging Laboratory, Department of Electrical Engineering, California Institute of Technology, Pasadena, CA, USA. [3]These authors contributed equally: Yang Zhang, Joshua Olick-Gibson. e-mail: lvw@caltech.edu

signals within the lumen of a vessel are suppressed relative to the signals at the boundaries due to the random summation of absorption signals from millions of RBCs in each lumen imaging voxel, thus rendering PACT as 'speckle-free'[14]. While recent work has utilized PACT speckle field decorrelation to extract velocity measurements in ink phantoms and chicken embryos, direct imaging of blood flow beyond the optical diffusion limit has remained elusive[15].

In this Article, we report photoacoustic vector tomography (PAVT) as a framework for obtaining vector maps of human blood flow by photoacoustics beyond the optical diffusion limit. The key features of this framework can be summarized as follows: (1) The synergy between the spatial heterogeneity of blood and the photoacoustic contrast produces strong photoacoustic signals in the lumen of the blood vessels. (2) Successive compilation of single-shot, wide-field photoacoustic images allows for the direct visualization of blood flow throughout the lumen. (3) Applying pixel-wise motion estimation algorithms to the reconstructed images generates blood-flow vector maps with speed and direction quantification.

By means of simulation and validation in phantoms, we show that PAVT blood flow measurements are facilitated by the heterogeneity of blood. We assessed the accuracy of this measurement through trials on ex vivo blood in which measured flow speeds were validated against known values. We acquired images in the vessels of the hand and arm regions of healthy participants using a linear ultrasound array probe coupled to an optical fibre bundle. We show in vivo that vector flow maps can be obtained in blood vessels greater than 5 mm in depth. We also show that vector flow imaging can be used to measure unique flow patterns at irregular interfaces in the blood vessel, such as valve regions. Lastly, we measured the in vivo functional PA blood flow responses to the inflation and release of a blood-pressure cuff. This work establishes PAVT as a viable imaging technique for the monitoring and diagnosis of vascular diseases and for the mapping of the function of the circulatory system.

Results

The principle of PAVT for deep haemodynamic imaging is illustrated in Fig. 1. Figure 1a shows the schematic of the system. An ultrasonic probe is placed on top of the skin and a laser delivers light through a fibre bundle to the blood vessels. The haemoglobin content within RBCs absorbs the light and converts it into heat. On the basis of the known photoacoustic effect, acoustic waves are generated through thermoelastic expansion and detected by the ultrasonic probe. The data are then streamed to the computer through the data acquisition (DAQ) module, and we employ the universal back projection algorithm[16] to reconstruct the images. Figure 1b illustrates the effect of blood heterogeneity (RBC spatial distribution) on the visibility of the signals arising from the lumen region of the blood vessel. For uniform blood, the simulated photoacoustic signals from the lumen region are suppressed relative to the signals at the boundaries (known as the boundary build-up effect[14]), resulting in little visibility in the lumen region of the image, whereas in non-uniform blood, the simulated photoacoustic signals from the lumen region show an increased amplitude, resulting in heightened visibility in the lumen region relative to the uniform case. Modelling of the spatial heterogeneity of blood and details about the simulation can be found in Methods and Supplementary Figs. 1–3. Figure 1c is a representative in vivo photoacoustic image of a blood vessel located beyond 1 mm depth. Similar to the simulated image in the non-uniform case, the in vivo image shows detectable signals from the lumen region of the blood vessel. To quantify the heterogeneity of the blood, we define a relative visibility index (γ) as $\frac{S_l - S_n}{S_b - S_n}$, where S_l denotes the mean lumen signal, S_b the mean boundary signal and S_n the mean background signal (Methods). The measured relative visibility index for the vessel in Fig. 1c is 0.15 ± 0.01 (n = 10). After acquiring multiple frames of data, we can clearly visualize the propagation of the lumen signals from frame to frame (Supplementary Video 1), as shown in the magnified view of the region in the white box in Fig. 1c (further data processing details can be found in Methods). We then apply a pixel-wise flow estimation algorithm to the images, extracting both the direction and magnitude of the blood flow inside the vessel. As shown in Fig. 1d, this map shows a laminar flow pattern in the lumen region, with a higher speed through the centre of the vessel and a lower speed at the edges.

To characterize the system resolution, we imaged a lead point source (actual diameter 50 µm). Figure 2a shows an axial resolution of 125 µm and a lateral resolution of 150 µm. To determine the mechanism for flow detectability and validate the speed estimation accuracy of PAVT, we designed a blood flow phantom to closely mimic in vivo circulation. Figure 2b shows the set-up for the flow phantom, in which a converging bifurcation is fabricated by two inlet channels (C_1 and C_2) feeding into an outlet channel (C_3). While imaging the outlet channel, five measured speeds were validated against preset syringe flow speeds. The results in Fig. 2c show strong agreement between the measured and preset values for all five speeds. These results were validated against Doppler ultrasound measurements (Supplementary Fig. 4) as well. In addition, we tested the limits of speed detection. The slowest measured flow was ~0.04 mm s^{-1}, while the fastest measured flow was ~100 mm s^{-1} (Supplementary Fig. 5). Finally, we found that the speed measurement is unaffected by the angle of the vessel relative to the probe (Supplementary Fig. 6). The mechanism for flow detectability is demonstrated in Fig. 2d–i. Figure 2d,f,h show the structural images of channels C_1, C_2 and C_3, respectively, before (top) and after (bottom) the induction of pressure fluctuations in the inlet channels, whereas Fig. 2e,g,i show the corresponding vector flow maps for each channel and scenario. Figure 2d–g show suppressed lumen signals and no flow detectability (97% relative error for measured mean speeds of 0.1 mm s^{-1} versus ground truth of 3.3 mm s^{-1}) in the inlet channels C_1 and C_2 with and without pressure fluctuations. The measured relative visibility index is 0.003 ± 0.007 (n = 40) for the bottom panel of Fig. 2d. In Fig. 2h (top), the structural image for outlet channel C_3 shows a detectable signal in the centre of the channel, which probably arises from the mixing of blood from each inlet channel, thus producing a detectable non-uniformity at the centre of the outlet channel. The vector flow image in Fig. 2i (top) shows weak flow detectability (80% relative error for measured mean speed of 0.6 mm s^{-1} versus ground truth of 3.3 mm s^{-1}). The measured relative visibility index is 0.098 ± 0.005 (n = 40) for Fig. 2h (top). After the induction of pressure fluctuations in the inlet channels, the structural image in Fig. 2h (bottom) shows the non-uniformity dispersed throughout the lumen region (Supplementary Video 2), allowing us to clearly track the flow (2.5% relative error for measured mean speed of 3.4 mm s^{-1} versus ground truth of 3.3 mm s^{-1}) in the vector flow map shown in Fig. 2i (bottom). The measured relative visibility index is 0.128 ± 0.006 (n = 40) for Fig. 2h (bottom). Thus, we conclude that the visibility of the photoacoustic lumen signals is enhanced by spatial heterogeneity in the blood.

Representative PAVT images of four blood vessels at depths beyond the optical diffusion limit are shown in Fig. 3. Figure 3a shows a vessel in the wrist (Supplementary Video 3), imaged at an optical wavelength (λ) of 1,064 nm and a pulse repetition frequency (PRF) of 100 Hz. The vessel has a varying diameter along its longitudinal axis with a high flow speed in the upstream narrower region (probably due to smooth-muscle contraction) and a lower flow speed in the downstream dilated region. Figure 3b shows a vessel in the palmar region imaged at a PRF of 100 Hz with an isosbestic wavelength (805 nm) of oxy- and deoxyhaemoglobin (Supplementary Video 4). Demonstration of flow measurements at other wavelengths can be found in Supplementary Fig. 7 and Video 5. In Fig. 3c,d, the structural images of two different forearm vessels acquired at λ = 1,064 nm and PRF = 20 Hz show that the distances from the skin surfaces to the axes of the vessels are 3.5 mm and 5.5 mm, respectively, with the vector maps confirming that the blood flow is still detectable (Supplementary Videos 6 and 7). For Fig. 3c,d, the measured signal-to-noise ratio values at the centre

https://doi.org/10.1038/s41551-023-01148-5

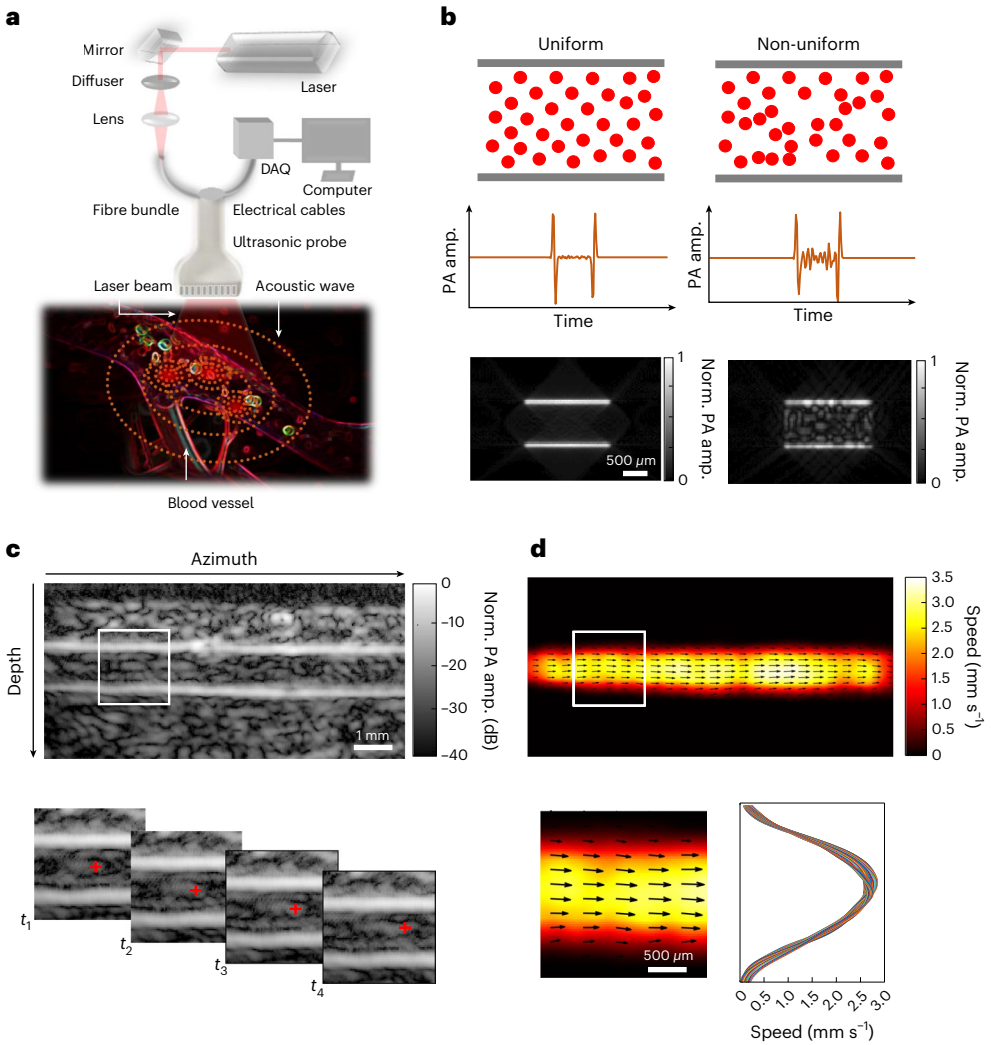

Fig. 1 | PAVT. a, Schematic of the imaging system. Light from a laser is delivered to the blood vessel region via a fibre bundle. Photoacoustic waves are generated and then detected by the ultrasonic probe. Photoacoustic signals are streamed to the computer through the DAQ module. **b**, Effect of blood heterogeneity on the visibility of the signals arising from the lumen region of the blood vessel. For uniform blood, the simulated photoacoustic signals from the lumen region are suppressed relative to the signals at the boundaries, resulting in little visibility in the lumen region of the image, whereas in non-uniform blood, the simulated photoacoustic signals from the lumen region show an increased amplitude, resulting in heightened visibility in the lumen region relative to the uniform case. **c**, Top: structural images of a blood vessel are reconstructed in real time. Bottom: magnified view of the region in the white box in the top image shows that the image features in the lumen region (beyond 1 mm depth) can be tracked in successive images at timepoints t_1 to t_4. **d**, Top: reconstruction of a blood flow speed map after tracking all of the features in the field of view. Bottom right: quantitative representation of the flow vector fields overlaid on the speed map. Bottom left: magnified view of the region in the white box in the top image shows that the flow has a laminar pattern.

of vessel lumen regions were 14.1 and 5.8, respectively, whereas the contrast-to-noise ratio values were 7.1 and 2.5, respectively. In vivo validation of PAVT with ultrafast Doppler ultrasound can be found in Supplementary Fig. 8.

A carpal tunnel vein with a valve is shown in Fig. 4 (Supplementary Video 8), as indicated by the white circles in Fig. 4a. The vector maps and speed profiles in Fig. 4b,c and d, respectively, indicate a higher speed in the narrow-diameter intra-valve region and lower speeds in the wider-diameter regions surrounding the valve. In Fig. 4e,f, magnified views of the regions indicated by the white boxes show a converging flow pattern within the valve. Furthermore, the magnified vector maps highlight the sinus pocket regions[17] above and below the valve boundaries, as shown by the dashed lines in Fig. 4e,f.

To evaluate functional changes, we measured a participant's blood flow before, during and after inflating a blood-pressure cuff. The cuff was placed against the brachial vein in the upper left arm, and the imaged vessel was located in the metacarpal region, distal to the application site of the cuff. Fractional speed changes were measured relative to the baseline flow. Figure 5 shows a flow speed decrease of ~70% while the cuff was inflated, followed by a transient flow speed increase of ~350% upon release of the cuff and eventually a steady-state return to the baseline (Supplementary Video 9). The 70% drop can be explained by incomplete cuffing, whereas the transient increase could be due to an immediate pressure release in the metacarpal vessel. This experiment was repeated for multiple participants, with flow speed responses reported in Supplementary Fig. 9.

Discussion

We have shown that photoacoustics can be used to image human blood flow beyond the optical diffusion limit. Through phantom experiments, we validated the mechanism and accuracy of this measurement. By employing in vivo vector flow analysis, we have demonstrated the versatility of PAVT across laser PRF, laser wavelength and depths. Furthermore, we have shown that in the vicinity of valves PAVT can

https://doi.org/10.1038/s41551-023-01148-5

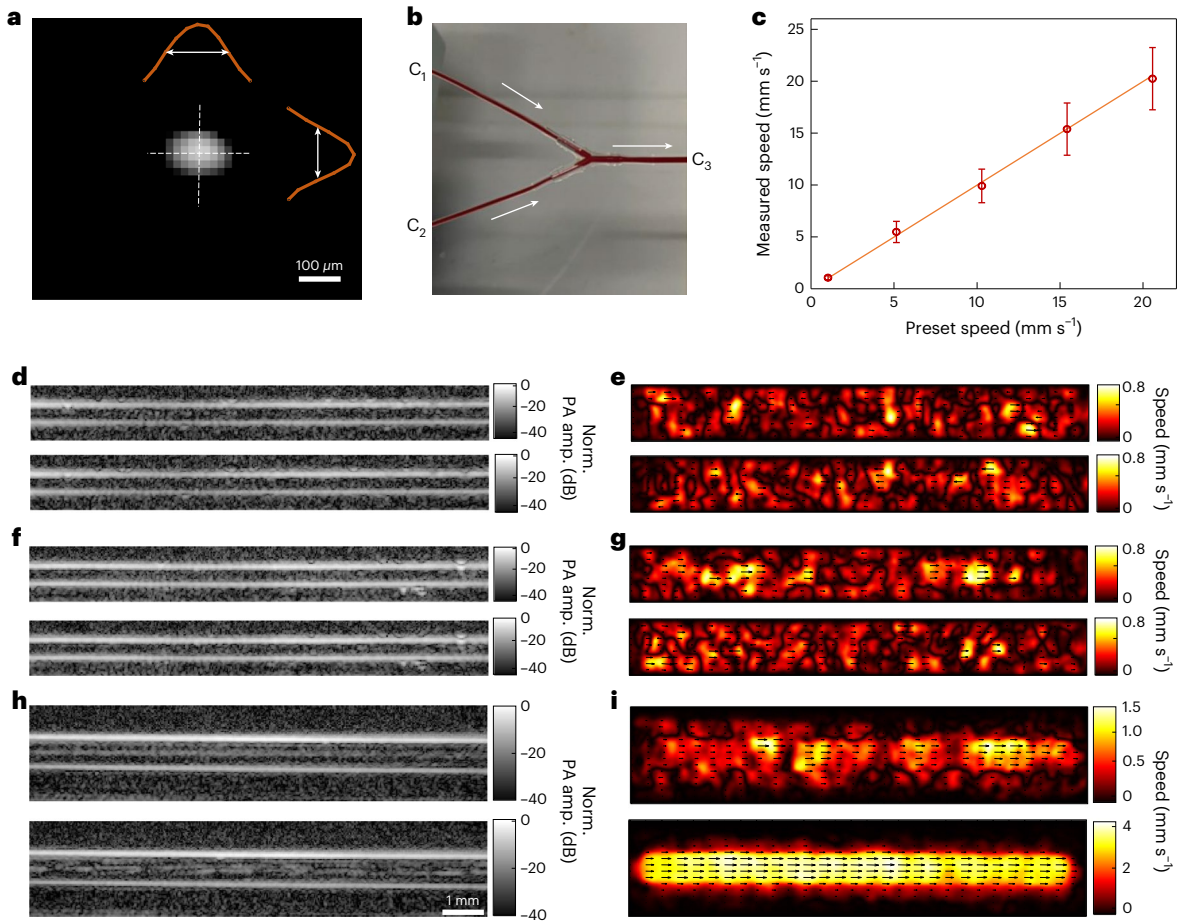

Fig. 2 | System characterization and phantom validation. a, Image of a lead point source (actual diameter 50 μm), showing axial and lateral resolutions of 125 and 150 μm, respectively. **b**, Blood phantom set-up with inlet channels C_1, C_2 and outlet channel C_3. **c**, Measured flow speeds plotted against preset syringe flow speeds. The mean ± s.d. (in mm s^{-1}) speeds were (from left to right): 1.07 ± 0.21, 5.33 ± 0.85, 9.93 ± 1.83, 14.77 ± 2.76 and 20.14 ± 3.17 with relative errors of 4.5, 3.6, 3.4, 4.2 and 2.0 %, respectively (n = 6,859). Orange line represents the preset speed. **d**,**f**,**h**, Structural images in channels C_1, C_2 and C_3, respectively, before (top) and after (bottom) the induction of pressure fluctuations. **e**,**g**,**i**, Vector flow maps in channels C_1, C_2 and C_3, respectively, before (top) and after (bottom) the induction of pressure fluctuations.

measure flow patterns that deviate from typical laminar flow. In tracking the flow speed changes in response to a blood-pressure cuff, we have established PAVT as a powerful imaging technique that can perform functional measurements of blood flow in deep vessels. As such, PAVT outperforms existing purely optical methods for deep haemodynamic imaging and complements ultrasound imaging[18–20] by simultaneously providing haemoglobin-based molecular contrast[21].

There is an inherent trade-off between imaging depth and laser PRF. For instance, the American National Standards Institute's (ANSI) safety limit for skin exposure at a laser wavelength of 1,064 nm is 50 mJ cm^{-2} and 10 mJ cm^{-2} at a laser PRF of 20 Hz and 100 Hz, respectively[22]. Therefore, if one wishes to maximize laser fluence to image deep blood vessels with a high signal-to-noise ratio, one must necessarily decrease the laser PRF to satisfy the ANSI limit. This trade-off is exemplified in Fig. 3, in which we used a 20-Hz laser PRF to image blood flow at a depth of ~5.5 mm (Fig. 3d), whereas we used a 100-Hz laser PRF to image blood flow at a depth of ~1.5 mm (Fig. 3a). The effect of the frame rate on speed estimation is further expounded in Supplementary Fig. 10. Starting with a dataset acquired at a 100-Hz PRF over 1 s, we downsampled the images at effective frame rates of 50, 20, 10 and 5 Hz. The mean speeds showed reasonable agreement (within 1 s.d. of the 100-Hz upsampled mean speed), at frame rates of 50, 20 and 10 Hz, with an underestimation at 5 Hz (relative error of 89%). These results are consistent with equation (8), in which the calculated flow pattern correlation length and flow speed of ~0.6 mm and 2 mm s^{-1}, respectively, correspond to a minimum required laser PRF of 6.7 Hz according to the Nyquist sampling theorem[23].

To clearly visualize the flow, we employed two post-processing techniques before velocity quantification. First, we implemented a singular value decomposition (SVD)-based spatiotemporal filter to the reconstructed photoacoustic images to extract the dynamic features (that is, blood flow). Next, we applied amplitude-based logarithmic compression[24] to the filtered images to highlight the lumen signals. As shown by the dashed lines in Supplementary Fig. 11, each of these steps may be implemented individually or together. The accuracy of these methods is demonstrated in Supplementary Fig. 12, in which we consider a representative phantom dataset. The relative errors for Supplementary Fig. 12a–d were 29, 6.9, 1.4 and 0.3%, respectively, indicating that implementing SVD and logarithmic compression yields the most accurate results, albeit with modest improvement over implementing logarithmic compression without SVD.

In addition, we applied a pixel-wise noise floor filtering method (details in Methods) before generating the final vector flow maps. The effect of this procedure is demonstrated in Supplementary Fig. 13, in which we consider a phantom dataset with a mean flow speed of 4.11 mm s^{-1} as the ground truth. Supplementary Fig. 13a shows the estimated speed map when averaging across all frames for each pixel, yielding a calculated mean speed of 3.93 mm s^{-1} (relative error of 4.5%). This

https://doi.org/10.1038/s41551-023-01148-5

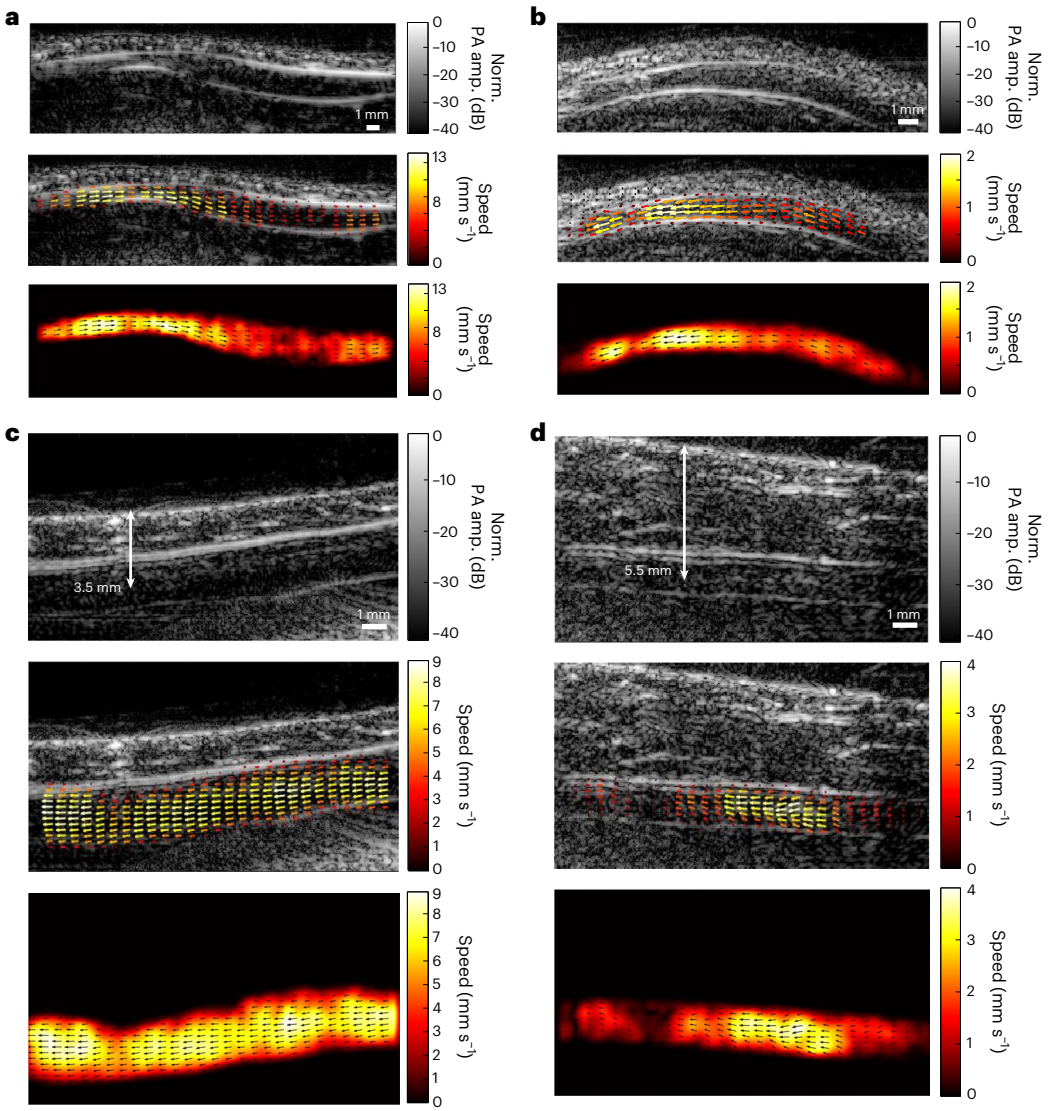

Fig. 3 | PAVT vector flow maps. a, Structural image (top), overlaid vector flow map (middle) and vector flow map (bottom) of a vessel in the wrist with a varying diameter. **b**, Structural and vector maps of a vessel in the palmar region imaged at an isosbestic wavelength for oxygenated and deoxygenated haemoglobin (805 nm). **c**,**d**, Structural and vector maps of vessels in the forearm imaged at 3.5- and 5.5-mm depths, respectively.

underestimation is because when calculating pixel-wise frame-to-frame motion, low-speed noise measurements may erroneously be incorporated into the velocity quantification due to spatial gaps in the propagating flow pattern (as shown in the bottom panel of Fig. 2h). To avoid this underestimation, we calculated the temporal standard deviation of each pixel's speed measurements to form a pixel-wise noise floor, below which frames with low speeds (that is, measurements due to noise) were excluded. Supplementary Fig. 13b shows the estimated speed map when averaging across the remaining frames, yielding a calculated mean speed of 4.07 mm s^{-1} (relative error of 0.9%).

An important aspect of PAVT is that it can detect variations in flow patterns throughout the lumen of the blood vessel. Figure 4 highlights key features regarding the detectability of PAVT in blood vessel regions containing valves. From a structural standpoint, it is important to note that the valves in the venous extremities, such as the one imaged in this work, are composed of endothelial cells and connective tissue[25], for which photoacoustic imaging does not have high contrast relative to haemoglobin. However, similar to the walls of the blood vessels, the valve can be considered as a sub-boundary of the blood, and we can detect the sub-boundaries of these structures due to the boundary build-up effect. Our PAVT images reveal that we can detect complex vector flow patterns in the regions surrounding the valves, and our speed profiles in Fig. 4d are consistent with that predicted by the continuity equation[26], showing a higher speed in the narrow-diameter intra-valve region and lower speeds in the wider-diameter regions before and after the valve (relative error of 3.2%). We also demonstrated the ability to measure temporal changes in the flow speed due to the application of a blood-pressure cuff, thus establishing a basis for detecting functional responses. Furthermore, we observed naturally occurring temporal blood flow changes in a vertically oriented hand, possibly due to the counteracting force of gravity against the venous one-way valves (Supplementary Video 12).

Here we consider the most likely hypothesis for the mechanism of blood flow detectability by PAVT. We designed a flow phantom (Fig. 2) to closely mimic in vivo circulation, this phantom consisting of a converging bifurcation that has two inlet channels and an outlet channel with diameters roughly corresponding to Murray's law[27] (that is, the cubic of the vessel radius r is conserved: $r^3_{out} = r^3_{in1} + r^3_{in2}$, where 'out' denotes the outgoing branch and 'in1' and 'in2' denote the two incoming branches, respectively). Because whole blood is uniform, we were unable to image baseline blood flow in either of the inlet channels.

https://doi.org/10.1038/s41551-023-01148-5

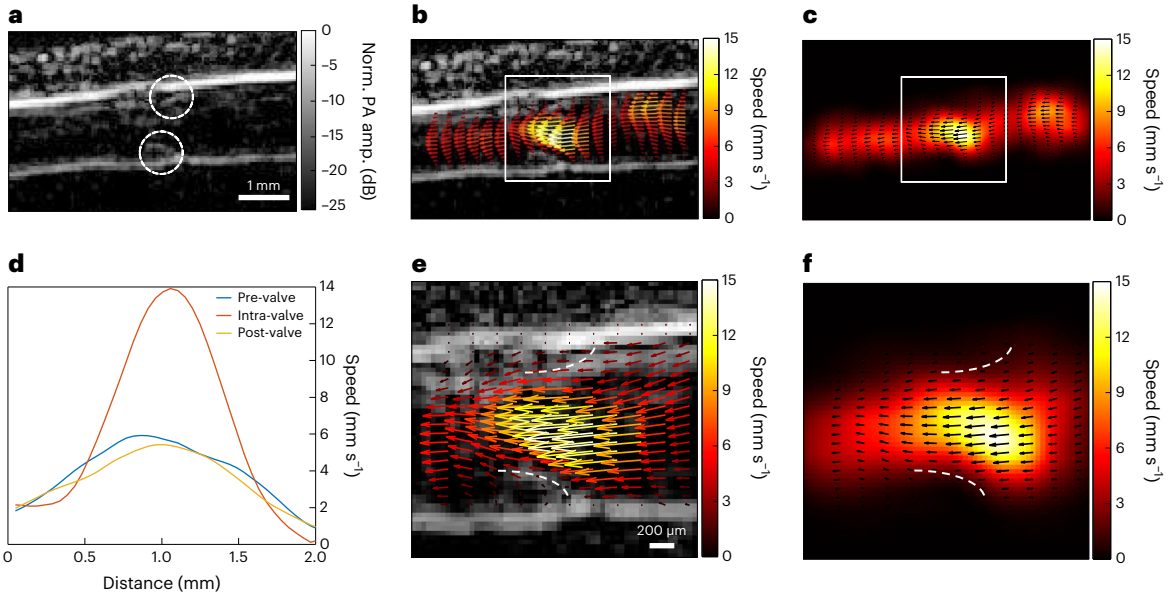

Fig. 4 | PAVT characterization of haemodynamics around a valve. a, A venous valve in the carpal tunnel region in the arm (valve boundaries indicated by white circles). **b**,**c**, Vector overlay and vector flowmaps, respectively, showing a higher speed inside the valve region than the regions upstream and downstream of the valve. **d**, Speed profiles taken upstream, within and downstream of the valve (pre-valve, intra-valve and post-valve, respectively). **e**,**f**, Magnified views of the maps in **b** and **c**, with the valve boundaries indicated by the dashed white lines.

However, as shown in the top panel of Fig. 2h, the converging bifurcation produced a detectable non-uniformity of RBC distribution in the centre of the outlet channel. Furthermore, inducing pressure fluctuations in the inlet channels resulted in the dispersion of this non-uniformity throughout the lumen of the outlet channel, allowing us to clearly visualize the blood flow. From a physiological perspective, converging bifurcation structures merging dissimilar blood naturally occur throughout the venous system[28] and pressure fluctuations can be induced by the opening and closing of one-way valves in the veins, as well as by smooth-muscle contractions. In validating the flow speed measurements with the preset syringe flow speeds, we hypothesize that the two aforementioned factors facilitate in vivo flow measurement by inducing blood spatial heterogeneity that is detectable at our probe's centre frequency.

For completeness, we also consider the hypothesis that PAVT flow measurement is facilitated by the propagation of oxygen saturation (sO_2) heterogeneities. This hypothesis is reasonable due to PA's selective contrast to oxy- and deoxyhaemoglobin at most wavelengths. However, as shown in Fig. 3, we were able to measure flow even at an isosbestic wavelength of 805 nm, effectively ruling out this hypothesis.

Moreover, we demonstrated that PAVT blood flow measurement is versatile, with consistent speed measurements across three different laser wavelengths (750 nm, 805 nm and 900 nm) in the near-infrared spectral region (Supplementary Fig. 7) while imaging a palmar vein, indicating that spectral PAVT measurement of blood flow and sO_2 is achievable. The sO_2 and blood flow maps of vessels in three different regions are shown in Supplementary Fig. 14. Using linear unmixing with surface fluence compensation[29] for each vessel, we calculated sO_2 values of 66, 73 and 65%, respectively, which agree with accepted literature values in healthy participants[30]. While methods such as Doppler ultrasound and pulse oximetry can each individually image blood flow and sense systemic arterial oxygen saturation without imaging, respectively, PAVT can simultaneously image these physiological parameters, which can provide crucial information regarding brain function[31] and hallmarks of cancer, such as angiogenesis and hypermetabolism[32]. In addition to providing simultaneous sO_2 and blood flow measurements, PAVT may have clinical advantages over Doppler ultrasound due to its angle independence, as shown in Supplementary Fig. 6. Furthermore, PAVT has the ability to measure extremely slow flow (relative error of 4.3% for measured speed of 0.039 mm s^{-1} versus a ground truth of 0.041 mm s^{-1}), as shown in Supplementary Fig. 5. Doppler ultrasound, on the other hand, is unable to measure flow that is this slow (relative error of >100% for measured speed of 0.41 mm s^{-1} versus a ground truth of 0.041 mm s^{-1}).

Although we have shown that PAVT can be efficacious in veins, there remains an outstanding hurdle to image blood flow in arteries. Our hypothesis for the inability to measure arterial flow relates to the visibility of the lumen–blood signals. For PAVT flow measurement, two factors are required: a sufficient visibility of the lumen–blood signals and a sufficient imaging frame rate to track the movement. It is known that arterial flow is, on average, faster than venous flow. Although the speed of blood certainly affects whether we can accurately measure blood flow at a given imaging frame rate, it is not directly related to flow visualization. As shown in our arterial images (Supplementary Fig. 15, and Videos 10 and 11), we cannot visualize the lumen signals, which means that there would not be a sufficient signal to track even if the blood flow was slowed down. The measured relative visibility indices for the arteries in Supplementary Fig. 15a,c were 0.008 ± 0.010 (n = 10) and 0.002 ± 0.004 (n = 10), respectively, which are much lower than those in the vein, that is, 0.15 ± 0.010 (n = 10) in Fig. 1. These results confirm the insufficient heterogeneity of the arterial lumen signals relative to that of the veins. Furthermore, as shown in our phantom experiment (Supplementary Fig. 5), we measured blood flow as fast as 100 mm s^{-1}, which should be sufficient for many arteries in the regions that we imaged. Together, these results support our hypothesis that the limiting factor for PAVT arterial flow measurement is the visibility of the lumen signals, rather than the speed of the blood. From a physiological perspective, this hypothesis is reasonable because by the time blood from the venous circulation returns to the heart and transitions to the arterial circulation, the blood has become well-mixed and more uniform. As such, the spatial heterogeneity that highlights the photoacoustic signals in the venous blood is no longer present.

In its current stage, PAVT may be capable of clinical implementation, as it extends the photoacoustic blood flow measurement to five times beyond the optical diffusion limit. In principle, PAVT is not limited

https://doi.org/10.1038/s41551-023-01148-5

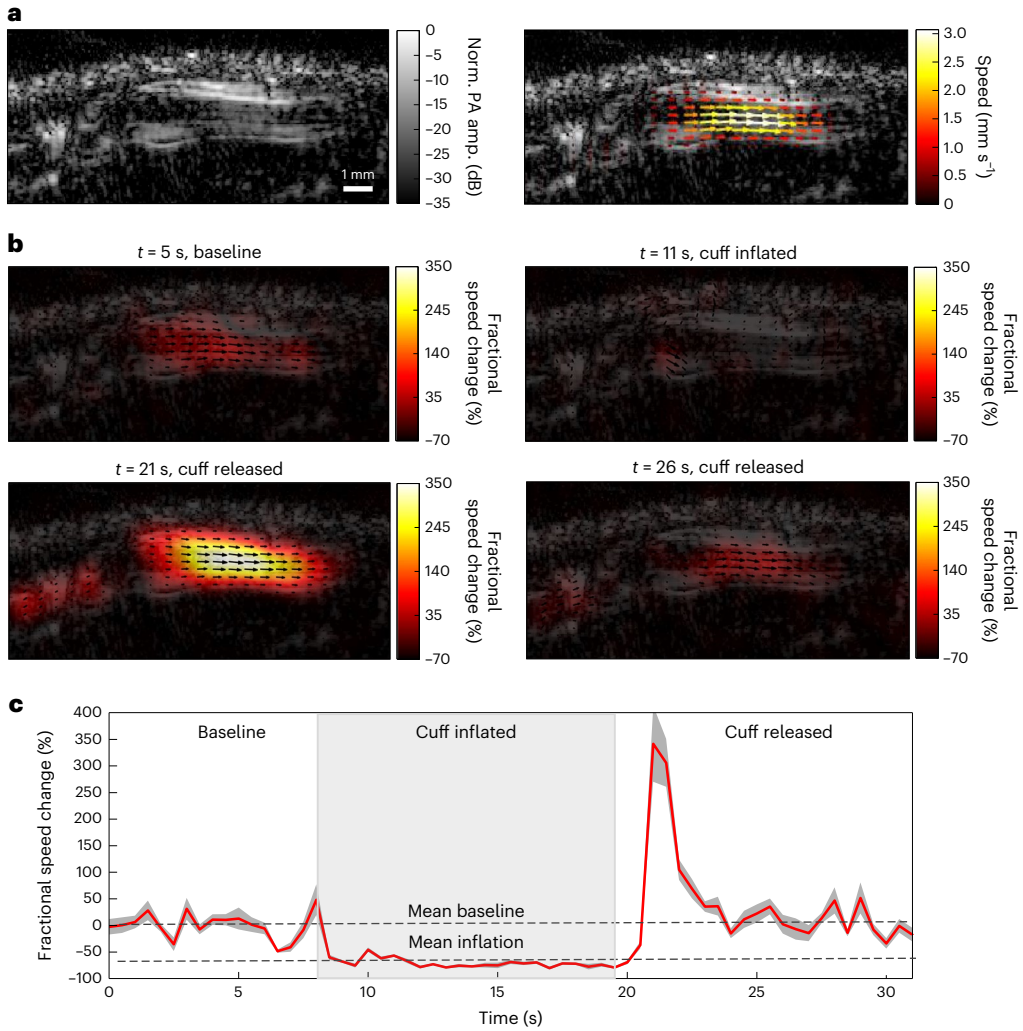

Fig. 5 | Measuring functional responses to a blood-pressure cuff. A blood-pressure cuff was applied to the upper left arm across the participant's brachial vein. Baseline flow was measured in a distal metacarpal vein, after which subsequent flow measurements were quantified relative to the mean of this baseline. The cuff was inflated for ~10 s before release. **a**, Structural image of the vessel (left) and the vector overlay map for the baseline flow speed (right). **b**, Vector maps for relative flow measurements at four different timepoints throughout the experiment: the baseline flow (top left), the flow during cuff inflation (top right), the flow during release (bottom left) and the flow after release (bottom right). **c**, Discrete-time sequence for relative flow speed changes. The flow speed decreased by ~70% during the application of the cuff and increased to ~350% upon release before returning to baseline.

to the linear array probe that we employed in this work. As such, future work may extend this technique to other array geometries such as the ring array and hemispherical array that provide more complete acoustic views for enhanced image quality. Specifically relevant to this study, peripheral vascular diseases such as chronic venous insufficiency[33] and varicose veins[33] can be diagnosed by imaging blood flow in the extremities. Future studies may also extend this approach to other regions of the human body for applications such as breast cancer[34] and functional brain imaging[35,36].

Although veins carry ~75% of the total blood volume in the circulatory system, measuring blood flow in both veins and arteries provides more complete clinical information for diagnosing and preventing disease. The clinical impact of this technique will be fully realized when we can perform metabolic imaging of physiological systems. The metabolic rate of oxygen consumption (MRO_2)[37] for a system can be estimated by measuring the blood flow, total haemoglobin concentration and oxygen saturation of the major input and output vessels (that is, arteries and veins, respectively). Although in its current state, PAVT can only measure blood flow in veins, the principle of mass conservation can be applied to estimate the arterial inflow rate from the venous outflow rate. As such, metabolic imaging with PAVT may be a not-so-distant clinical possibility. For example, early breast cancer detection can be aided by monitoring tumour-induced changes in MRO_2 (ref. 34).

PAVT extends the depth of photoacoustic blood flow measurement to five times further than what was previously considered possible. However, there will always be a clinical need to push this limit even further. In this work, we employed a 15-MHz probe to image blood flow within 5 mm depth. Extending this depth further is primarily limited by the acoustic attenuation arising from the high centre frequency of our probe, as well as by the fact that the vessel lumen signal is weaker than the boundary signal. Future work should therefore explore the implementation of lower-frequency probes to image blood flow at centimetre-level depth at the expense of lower resolution. If the spatial heterogeneity of blood becomes unresolvable, its detectability may decrease. As such, PAVT may eventually provide simultaneous measurements of cerebral blood flow, haemoglobin concentration and oxygen saturation for functional human brain imaging. Furthermore, centimetre-level depth would enable imaging of both the carotid artery and the jugular vein, thus making cerebral metabolic imaging possible.

Methods

System construction

We employed a 256-element linear ultrasonic transducer array (LZ250, VisualSonics) for photoacoustic signal detection at a centre frequency of 15 MHz. The transducer array has a size of 23 mm × 3 mm and each element of the array has a cylindrical focus with a 15-mm focal length. The ultrasound probe was directly connected to the 256 DAQ channels of the Verasonics Vantage 256 system (Verasonics; 14-bit A/D converters; 62.5 MHz sampling rate; programmable gain up to 51 dB) through a UTA 360 connector. The photoacoustic signals were acquired and digitized into local memory and then transferred to a host computer via PCI express.

For light delivery, we incorporated an optical fibre bundle with the ultrasound probe. The fibre bundle and the array were coaxially aligned to maximize the system's performance. At the front end of the fibre bundle, a 1,064-nm-wavelength laser beam (Quantel Brilliant B pulsed YAG laser, 10 Hz, 5–6 ns pulse width; Quantel Q-Smart 450 laser, 20 Hz, 5–6 ns pulse width) or a 670 nm–1,070 nm laser beam (SpitLight EVO III, InnoLas Laser; 100 Hz, 5–8 ns pulse width) was utilized to pass through the fibre bundle and was delivered to the imaging target. The angle of incidence of the beam was 30 degrees relative to the imaging plane. The optical fluences were ~50 mJ cm^{-2} for the 1,064 nm wavelength at 10 Hz PRF, 30 mJ cm^{-2} at 20 Hz PRF and 6 mJ cm^{-2} at 100 Hz PRF, which were less than the safety limit set by the ANSI (100 mJ cm^{-2}, 50 mJ cm^{-2}, 10 mJ cm^{-2}, respectively, and 1,000 mW cm^{-2})[22].

To synchronize the system, the laser's flashlamp trigger was used to trigger the DAQ for photoacoustic signal acquisition. For each laser pulse, we acquired both the signal from the ultrasound probe surface and the signal from the imaging target. We then corrected the delay and jitter between the DAQ and the laser system using the acquired surface signal. The preprocessed raw signals were then back-projected to reconstruct the two-dimensional (2D) photoacoustic image.

Data acquisition

For the human imaging set-up, we prepared a portable water tank and placed it on top of the table. The ultrasound probe was mounted on a 3D linear stage with its surface immersed in the water tank. The human hand/arm region was placed below the probe surface and coupled in water with the ultrasound probe. We implemented the photoacoustic imaging sequence to monitor the blood vessel in real time. We achieved a frame rate of 10 Hz, 20 Hz or 100 Hz corresponding to the laser PRF. In the blood-pressure-cuff experiment, a blood-pressure cuff device (GF Health Products) was placed on the upper arm region. The total acquisition took 30 s, with a baseline of ~5 s at the beginning, a subsequent cuff period of ~10 s and a release of ~15 s.

In the phantom validation experiments, the flow phantom was constructed using micro-renathane tubing (BrainTree Scientific). Each inlet channel had an inner diameter of 0.6 mm, and the outlet channel had an inner diameter of 1.0 mm. The phantom was perfused with 45% haematocrit whole bovine blood (QuadFive). Pressure fluctuations were induced by gently squeezing the inlet channels.

Ultrafast ultrasound Doppler imaging was implemented by coherent plane wave compounding[38,39] with seven tilted plane waves from −14 degrees to +14 degrees at a PRF of 10,000 Hz. The Doppler flow maps were generated using a vector projectile imaging framework[40,41]. Briefly, for each plane wave angle, we obtained the conventional colour Doppler image, after which we used least-squares multi-angle Doppler estimators to form the final flow images. In the ultrasound validation experiment, the ultrafast ultrasound data were immediately acquired after the PAVT imaging sequence to ensure the same state in the region of interest.

Data processing

To visualize the blood flow and obtain the vector flow map from the acquired raw photoacoustic signals, we used the following procedure for data processing (Supplementary Fig. 11). We first applied a universal back-projection image reconstruction algorithm[16] to the raw photoacoustic signals to reconstruct the images. We then logarithmically compressed the reconstructed structure images of the blood vessel (that is, structure images in Figs. 1–5) to directly visualize the blood flow (that is, the top panel of Supplementary Videos 1, 3, 4, 6–8, 10 and 11). For clearer blood flow visualization, we applied an SVD-based spatiotemporal filter to the reconstructed images and then performed logarithmic compression on the filtered images (that is, the bottom panel of Supplementary Videos 1, 3, 4, 6–8, 10 and 11). Lastly, we used a pixel-wise flow estimation method (see below) and noise floor filtering to obtain the velocity of the blood flow. For each pixel, the frame-to-frame velocity was estimated to form a 3D velocity structure with two spatial axes (ultrasound probe azimuthal direction x and axial direction z) and one time axis (time t). The temporal standard deviation of each pixel's speed measurements was calculated to form a pixel-wise noise floor, below which frames with low speeds (that is, measurements due to noise) were excluded. The final velocity map was constructed from averaging the remaining frames across the temporal domain. For all calculations of speed standard deviations performed in this work, an $m \times n$ region of interest in the vessel was segmented into m profiles, with each profile being parallel to the vessel's longitudinal axis. We then calculated the spatial standard deviation along each profile (σ_i) and found the final standard deviation (σ_{final}) by taking the mean of the profiles' standard deviations: $\sigma_{\text{final}} = \frac{1}{m}\sum_{i=1}^{m}\sigma_i$.

In PAVT, a spatiotemporal filter is used to extract the blood component from the structural images. In our case, the spatiotemporal structure dataset had three dimensions with two spatial axes (ultrasound probe azimuthal direction x and axial direction z) and one time axis (time t). We first reshaped the 3D dataset into a 2D space–time matrix $S_{\text{structure}}(x,z,t)$. Then we used SVD[42] to decompose the data matrix as follows:

$$S_{\text{structure}}(x,z,t) = \sum_{i=1}^{r}\sigma_i u_i(x,z)v_i^{\mathrm{T}}(t), \tag{1}$$

where r is the rank of the data matrix, σ_i is the i^{th} singular value, T is the conjugate transpose, $u_i(x,z)$ corresponds to the spatial domain, and $v_i(t)$ corresponds to the temporal domain. The static or slow-moving components (that is, tissue) correspond to the first few larger singular values. Therefore, the relatively fast-moving blood components can be extracted as

$$S_{\text{blood}}(x,z,t) = S_{\text{structure}}(x,z,t) - \sum_{i=1}^{\lambda}\sigma_i u_i(x,z)\,v_i^{\mathrm{T}}(t) \tag{2}$$

where λ is the cut-off of the singular values for extracting the blood component. Finally, the filtered 2D space–time matrix $S_{\text{blood}}(x,z,t)$ was reshaped back to 3D with the same size as the original 3D dataset.

For flow estimation, the Farneback method[43] for optical flow was employed. Briefly, the Farneback method approximates pixel neighbourhoods as polynomial expansions. By assuming a constant intensity of the displaced neighbourhoods between adjacent frames, the displacement field is estimated as follows. Let the pixel neighbourhood in Frame 1 at position vector $\mathbf{x}$ be approximated as:

$$f_1(\mathbf{x}) = \mathbf{x}^{\mathrm{T}}A_1\mathbf{x} + \mathbf{b}_1^{\mathrm{T}}\mathbf{x} + c_1, \tag{3}$$

in which the coefficients A_1 (a symmetric matrix), $\mathbf{b}_1$ (a vector) and c_1 (a scalar) are estimated by a weighted least-squares fit of the signal. Now, let the displaced pixel neighbourhood in Frame 2 be approximated as:

$$\begin{aligned} f_2(\mathbf{x}) = f_1(\mathbf{x}-\mathbf{d}) &= (\mathbf{x}-\mathbf{d})^{\mathrm{T}}A_1(\mathbf{x}-\mathbf{d}) + \mathbf{b}_1^{\mathrm{T}}(\mathbf{x}-\mathbf{d}) + c_1 \\ &= \mathbf{x}^{\mathrm{T}}A_1\mathbf{x} + (\mathbf{b}_1 - 2A_1\mathbf{d})^{\mathrm{T}}\mathbf{x} + \mathbf{d}^{\mathrm{T}}A_1\mathbf{d} - \mathbf{b}_1^{\mathrm{T}}\mathbf{d} + c_1 \\ &= \mathbf{x}^{\mathrm{T}}A_2\mathbf{x} + \mathbf{b}_2^{\mathrm{T}}\mathbf{x} + c_2 \end{aligned} \tag{4}$$

in which **d** is the displacement vector to be estim ated. By equating the coefficients

$$A_1 = A_2 \tag{5}$$

$$\mathbf{b}_2 = \mathbf{b}_1 - 2A_1\mathbf{d} \tag{6}$$

we solve for **d**:

$$\mathbf{d} = -\frac{1}{2}A_1^{-1}(\mathbf{b}_2 - \mathbf{b}_1) \tag{7}$$

Implementations of the Farneback method can be found in OpenCV and the Computer Vision Toolbox in MATLAB. Final flow maps were masked according to the pertinent vessel structure.

To track the movement of the blood using PAVT, the imaging frame rate f_{PRF} should satisfy the Nyquist sampling theorem[23,44], as determined by the equation below:

$$f_{PRF} > 2v/l, \tag{8}$$

where l is the correlation length of the blood signals and v is the blood flow speed. In other words, we must sample at least twice within the propagation time associated with the correlation length.

Spatial heterogeneity

Here, heterogeneity refers to the non-uniformity of the spatial distribution of RBCs in the vessel lumen. The concept of spatial heterogeneity is illustrated in Fig. 1b, in which we consider two scenarios. In the first scenario (Fig. 1b (left)), we modelled the spacing between the RBCs to be uniform and randomly distributed, yielding a weak lumen signal relative to the boundary signal in the PA image. In the second scenario (Fig. 1b (right)), the RBC spatial distribution was altered to be non-uniform and random. Without altering the global RBC concentration in the vessel, we induced local pockets of dense and sparse regions of the RBC distribution, yielding a more detectable lumen signal in the PA image. The variability in the heterogeneity was achieved by adjusting the local concentration differentials between the dense and sparse regions within the vessel. In detail, to model, simulate and measure the spatial heterogeneity of the blood, we defined our region of interest as a 3D volume with a size of r_x, r_y, r_z in the azimuthal, elevational and axial directions, respectively, of the ultrasonic probe (Supplementary Fig. 1). The spatial resolution cell is s_x, s_y, s_z in the corresponding directions, respectively. We can consider $r_y = s_y$ in the linear array probe case. Therefore, the number of divided subvolumes is

$$N_s = \frac{r_x r_z}{s_x s_z} \tag{9}$$

In the uniform case, the concentration of the RBCs in the N_s subvolumes are the same. Therefore, for a physiological concentration, C_p, of RBCs in a typical adult and a number concentration, C_i, of RBCs for each subvolume, we have

$$C_i = C_p, i = 1, 2, \ldots, N_s \tag{10}$$

Conversely, in the non-uniform case, the concentration of the RBCs in N_s subvolumes are different. On the basis of the haematocrit, H_t, of a typical adult, we can obtain the number concentration of RBCs for each subvolume as

$$\begin{cases} 0 \le C_i \le \frac{1}{H_t} C_p, i = 1, 2, \ldots, N_s \\ \frac{1}{N_s}\sum_{i=1}^{N_s} C_i = C_p \end{cases}. \tag{11}$$

Thus, $C_i = \lambda_i C_p$, with

$$\begin{cases} 0 \le \lambda_i \le \frac{1}{H_t}, i = 1, 2, \ldots, N_s \\ \frac{1}{N_s}\sum_{i=1}^{N_s} \lambda_i = 1 \end{cases}. \tag{12}$$

We can model λ_i as a uniform random distribution with mean $\mu = 1$ and scale parameter h_σ. Then we obtain

$$\begin{cases} \lambda_i = h_\sigma \eta_i + \frac{1}{2H_t} \\ \eta_i \sim \mathcal{U}_{[-\frac{1}{2H_t}, \frac{1}{2H_t}]} \end{cases}, \; i = 1, 2, \ldots, N_s \tag{13}$$

where h_σ is considered as the index for heterogeneity ranging from 0 to 1 and η_i is a uniform random distribution ranging from $-\frac{1}{2H_t}$ to $\frac{1}{2H_t}$. According to the typical haematocrit of a healthy adult, we chose $H_t = 50\%$, thus

$$\begin{cases} \lambda_i = h_\sigma \eta_i + 1 \\ \eta_i \sim \mathcal{U}_{[-1,1]} \end{cases}, \; i = 1, 2, \ldots, N_s \tag{14}$$

where η_i is a uniform random distribution from −1 to 1.

In the simulation study, we chose our total red blood cell concentration to match a typical physiological value of ~4.2×10^6 RBCs per ml of blood in the total lumen region of the vessel (1 mm in diameter) for both the uniform blood and non-uniform blood cases. The RBCs were distributed in a 2 mm × 1 mm × 1 mm 3D volume, which corresponds to the probe's azimuthal, elevational and axial directions, respectively. For the uniform blood case, the photoacoustic sources were randomly and uniformly distributed, with $h_\sigma = 0$. Conversely, in the case of non-uniform blood, the photoacoustic sources were randomly and non-uniformly distributed in the lumen region with dense and sparse local regions, which are determined by the heterogeneity index $0 < h_\sigma \le 1$. The simulation assumed a linear array ultrasound probe with the same centre frequency (15 MHz) and element arrangement (256 elements, 23 mm aperture size), as in the experimental case. We divided the 3D volume into 200 subvolumes with 100 µm × 100 µm × 1,000 µm, on the basis of the spatial resolution of the ultrasound probe.

We defined the relative visibility of the lumen signal as

$$\gamma = \frac{S_l - S_n}{S_b - S_n} \tag{15}$$

where S_l is the mean of the lumen signal, S_b is the mean of the boundary signal and S_n is the mean of the background signal outside the vessel region. The results in Supplementary Fig. 1 show that the relative visibility index γ obtained from the photoacoustic images has a linear one-to-one mapping relationship with the heterogeneity index h_σ, which determines the distribution of the RBCs. Thus, the measured visibility index γ was used to characterize the spatial heterogeneity from the phantom and in vivo experimental data.

To study the effect of varying the heterogeneity index and vessel diameter on the relative visibility, we simulated the following two cases. In the first case, we held the diameter of the vessel constant at 1.0 mm while varying the heterogeneity index across 12 levels from 0 to 1 (Supplementary Fig. 2). In the second case, we varied the diameter in 0.5 mm increments from 0.5 to 2.0 mm at heterogeneity indices of 0 and 0.5 for each diameter (Supplementary Fig. 3). The results show that the detected visibility of the lumen signal changes with the spatial heterogeneity condition of the blood but does not change with the vessel diameter.

Imaging protocols

The experiments on human extremities were performed in a dedicated imaging room. All experiments were performed according to

the relevant guidelines and regulations approved by the Institutional Review Board of the California Institute of Technology (Caltech). Eight healthy participants were recruited from Caltech. Written informed consent was obtained from all the participants according to the study protocols.

Reporting summary

Further information on research design is available in the Nature Portfolio Reporting Summary linked to this article.

Data availability

The data supporting the findings of this study are provided within the paper and its Supplementary Information. The raw and analysed datasets generated during the study are available for research purposes from the corresponding author on reasonable request.

Code availability

The reconstruction codes based on the universal back-projection algorithm are proprietary and used in licensed technologies, yet they are available from the corresponding author on reasonable request.

References

1. Won, R. Mapping blood flow. *Nat. Photonics* **5**, 393 (2011).
2. Rajan, V., Varghese, B., van Leeuwen, T. G. & Steenbergen, W. Review of methodological developments in laser Doppler flowmetry. *Lasers Med. Sci.* **24**, 269–283 (2009).
3. Leitgeb, R. A., Werkmeister, R. M., Blatter, C. & Schmetterer, L. Doppler Optical Coherence Tomography. *Prog. Retin. Eye Res.* **41**, 26–43 (2014).
4. Qureshi, M. M. et al. Quantitative blood flow estimation in vivo by optical speckle image velocimetry: publisher's note. *Optica* **8**, 1326 (2021).
5. Boas, D. A. & Dunn, A. K. Laser speckle contrast imaging in biomedical optics. *J. Biomed. Opt.* **15**, 011109 (2010).
6. Cinotti, E. et al. Quantification of capillary blood cell flow using reflectance confocal microscopy. *Skin Res. Technol.* **20**, 373–378 (2014).
7. Wang, L. V. & Hu, S. Photoacoustic tomography: in vivo imaging from organelles to organs. *Science* **335**, 1458–1462 (2012).
8. Wang, L. V. Tutorial on photoacoustic microscopy and computed tomography. *IEEE J. Sel. Top. Quantum Electron.* **14**, 171–179 (2008).
9. Yao, J. et al. High-speed label-free functional photoacoustic microscopy of mouse brain in action. *Nat. Methods* **12**, 407–410 (2015).
10. Kinnunen, M., Kauppila, A., Karmenyan, A. & Myllylä, R. Effect of the size and shape of a red blood cell on elastic light scattering properties at the single-cell level. *Biomed. Opt. Express* **2**, 1803–1814 (2011).
11. Wang, L. V. Multiscale photoacoustic microscopy and computed tomography. *Nat. Photonics* **3**, 503–509 (2009).
12. Brunker, J. & Beard, P. Velocity measurements in whole blood using acoustic resolution photoacoustic Doppler. *Biomed. Opt. Express* **7**, 2789–2806 (2016).
13. Yao, J. & Wang, L. V. Photoacoustic brain imaging: from microscopic to macroscopic scales. *Neurophotonics* **1**, 011003 (2014).
14. Guo, Z., Li, L. & Wang, L. V. On the speckle-free nature of photoacoustic tomography. *Med. Phys.* **36**, 4084–4088 (2009).
15. Pakdaman Zangabad, R. et al. Photoacoustic flow velocity imaging based on complex field decorrelation. *Photoacoustics* **22**, 100256 (2021).
16. Xu, M. & Wang, L. V. Universal back-projection algorithm for photoacoustic computed tomography. *Phys. Rev. E* **71**, 016706 (2005).
17. Lurie, F., Kistner, R. L., Eklof, B. & Kessler, D. Mechanism of venous valve closure and role of the valve in circulation: a new concept. *J. Vasc. Surg.* **38**, 955–961 (2003).
18. Szabo, T. L. *Diagnostic Ultrasound Imaging: Inside Out* (Academic Press, 2004).
19. Tanter, M. & Fink, M. Ultrafast imaging in biomedical ultrasound. *IEEE Trans. Ultrason. Ferroelectr. Freq. Control* **61**, 102–119 (2014).
20. Errico, C. et al. Ultrafast ultrasound localization microscopy for deep super-resolution vascular imaging. *Nature* **527**, 499–502 (2015).
21. Wang, L. V. & Wu, H. *Biomedical Optics: Principles and Imaging* (John Wiley & Sons, 2012).
22. American National Standards Institute. *American National Standard for the Safe Use of Lasers* ANSI z136.1–2014 (Laser Institute of America, 2014).
23. Cramer, H., & Grenader, U. The Nyquist frequency is that frequency whose period is two sampling intervals. *Probability and Statistics: The Harald Cramer Volume* p. 434 (Almqvist & Wiksell, 1959).
24. Lee, Y., Kang, J. & Yoo, Y. Automatic dynamic range adjustment for ultrasound B-mode imaging. *Ultrasonics* **56**, 435–443 (2015).
25. Fernández-Colino, A. & Jockenhoevel, S. Advances in engineering venous valves: the pursuit of a definite solution for chronic venous disease. *Tissue Eng. B Rev.* **27**, 253–265 (2021).
26. Petrila, T. & Trif, D. *Basics of Fluid Mechanics and Introduction to Computational Fluid Dynamics* (Springer Science & Business Media, 2004).
27. Murray, C. D. The physiological principle of minimum work. *Proc. Natl Acad. Sci. USA* **12**, 207–214 (1926).
28. Wiedeman, M. P. Dimensions of blood vessels from distributing artery to collecting vein. *Circ. Res.* **12**, 375–378 (1963).
29. Li, L. et al. Single-impulse panoramic photoacoustic computed tomography of small-animal whole-body dynamics at high spatiotemporal resolution. *Nat. Biomed. Eng.* **1**, 0071 (2017).
30. Keys, A. The oxygen saturation of the venous blood in normal human subjects. *Am. J. Physiol. Leg. Content* **124**, 13–21 (1938).
31. Na, S., Zhang, Y. & Wang, L. V. Cross-ray ultrasound tomography and photoacoustic tomography of cerebral haemodynamics in rodents. *Adv. Sci.* **9**, 2201104 (2022).
32. Yao, J., Maslov, K. I. & Wang, L. V. In vivo photoacoustic tomography of total blood flow and potential imaging of cancer angiogenesis and hypermetabolism. *Technol. Cancer Res. Treat.* **11**, 301–307 (2012).
33. Beebe-Dimmer, J. L., Pfeifer, J. R., Engle, J. S. & Schottenfeld, D. The epidemiology of chronic venous insufficiency and varicose veins. *Ann. Epidemiol.* **15**, 175–184 (2005).
34. Lin, L. & Wang, L. V. The emerging role of photoacoustic imaging in clinical oncology. *Nat. Rev. Clin. Oncol.* **19**, 365–384 (2022).
35. Na, S. et al. Massively parallel functional photoacoustic computed tomography of the human brain. *Nat. Biomed. Eng.* **6**, 584–592 (2022).
36. Zhang, Y. et al. Transcranial photoacoustic computed tomography of human brain function. Preprint at https://arxiv.org/abs/2206.00248 (2022).
37. Yao, J., Maslov, K. I., Zhang, Y., Xia, Y. & Wang, L. V. Label-free oxygen-metabolic photoacoustic microscopy in vivo. *J. Biomed. Opt.* **16**, 076003 (2011).
38. Montaldo, G., Tanter, M., Bercoff, J., Benech, N. & Fink, M. Coherent plane-wave compounding for very high frame rate ultrasonography and transient elastography. *IEEE Trans. Ultrason. Ferroelectr. Freq. Control* **56**, 489–506 (2009).
39. Zhang, Y., Guo, Y. & Lee, W.-N. Ultrafast ultrasound imaging with cascaded dual-polarity waves. *IEEE Trans. Med. Imaging* **37**, 906–917 (2018).
40. Yiu, B. Y., Lai, S. S. & Alfred, C. H. Vector projectile imaging: time-resolved dynamic visualization of complex flow patterns. *Ultrasound Med. Biol.* **40**, 2295–2309 (2014).

41. Dong, J., Zhang, Y. & Lee, W.-N. Walled vessel-mimicking phantom for ultrasound imaging using 3D printing with a water-soluble filament: design principle, fluid-structure interaction (FSI) simulation, and experimental validation. *Phys. Med. Biol.* **65**, 085006 (2020).
42. Demené, C. et al. Spatiotemporal clutter filtering of ultrafast ultrasound data highly increases Doppler and fultrasound sensitivity. *IEEE Trans. Med. Imaging* **34**, 2271–2285 (2015).
43. Farnebäck, G. Two-frame motion estimation based on polynomial expansion. In *Scandinavian Conference on Image Analysis* 363–370 (Springer, 2003).
44. Leis, J. W. *Digital Signal Processing Using MATLAB for Students and Researchers* (John Wiley & Sons, 2011).

Acknowledgements

We thank K. Maslov, L. Li and R. Cao for discussions about the flow mechanism; S. L. Spitalnik and P. Buehler for discussions about blood physiology; S. Davis and B. Park for discussion on the potential improvement of flow visualization; and L. Li for the suggestion about fibre coupling and assistance in light alignment. This work was sponsored by the United States National Institutes of Health (NIH) grants U01 EB029823 (BRAIN Initiative) and R35 CA220436 (Outstanding Investigator Award).

Author contributions

L.V.W., Y.Z. and J.O.-G. designed the study. Y.Z. and J.O.-G. built the system, analysed the data and wrote the paper with input from all authors. Y.Z., J.O.-G. and A.K. performed the experiments. L.V.W., Y.Z., J.O.-G. and A.K. interpreted the data. L.V.W. supervised the study and revised the paper.

Competing interests

L.V.W. has a financial interest in Microphotoacoustics Inc., CalPACT LLC and Union Photoacoustic Technologies Ltd. These companies did not provide support for this work. All other authors declare no competing interests.

Additional information

Supplementary information The online version contains supplementary material available at https://doi.org/10.1038/s41551-023-01148-5.

Correspondence and requests for materials should be addressed to Lihong V. Wang.

Peer review information *Nature Biomedical Engineering* thanks Jan Grimm, Ben McLarney, Chengbo Liu and Liming Nie for their contribution to the peer review of this work.

nature portfolio

Corresponding author(s): Lihong V. Wang

Last updated by author(s): Oct 23, 2023

Reporting Summary

Nature Portfolio wishes to improve the reproducibility of the work that we publish. This form provides structure for consistency and transparency in reporting. For further information on Nature Portfolio policies, see our Editorial Policies and the Editorial Policy Checklist.

Statistics

For all statistical analyses, confirm that the following items are present in the figure legend, table legend, main text, or Methods section.

n/a	Confirmed	
☐	☒	The exact sample size (*n*) for each experimental group/condition, given as a discrete number and unit of measurement
☐	☒	A statement on whether measurements were taken from distinct samples or whether the same sample was measured repeatedly
☒	☐	The statistical test(s) used AND whether they are one- or two-sided *Only common tests should be described solely by name; describe more complex techniques in the Methods section.*
☒	☐	A description of all covariates tested
☒	☐	A description of any assumptions or corrections, such as tests of normality and adjustment for multiple comparisons
☐	☒	A full description of the statistical parameters including central tendency (e.g. means) or other basic estimates (e.g. regression coefficient) AND variation (e.g. standard deviation) or associated estimates of uncertainty (e.g. confidence intervals)
☒	☐	For null hypothesis testing, the test statistic (e.g. *F*, *t*, *r*) with confidence intervals, effect sizes, degrees of freedom and *P* value noted *Give P values as exact values whenever suitable.*
☒	☐	For Bayesian analysis, information on the choice of priors and Markov chain Monte Carlo settings
☒	☐	For hierarchical and complex designs, identification of the appropriate level for tests and full reporting of outcomes
☒	☐	Estimates of effect sizes (e.g. Cohen's *d*, Pearson's *r*), indicating how they were calculated

Our web collection on statistics for biologists contains articles on many of the points above.

Software and code

Policy information about availability of computer code

Data collection	Matlab 2019a (MathWorks, Inc.). The data-collection software is used in licensed technologies, yet is available from the corresponding author on reasonable request.
Data analysis	Matlab 2021a (MathWorks, Inc.). The toolbox used to perform the frame-to-frame flow estimation is available in the Computer Vision Toolbox in Matlab 2021a. The reconstruction codes based on the universal backprojection algorithm are proprietary and used in licensed technologies, yet they are available from the corresponding author on reasonable request.

For manuscripts utilizing custom algorithms or software that are central to the research but not yet described in published literature, software must be made available to editors and reviewers. We strongly encourage code deposition in a community repository (e.g. GitHub). See the Nature Portfolio guidelines for submitting code & software for further information.

Data

Policy information about availability of data

All manuscripts must include a data availability statement. This statement should provide the following information, where applicable:

- Accession codes, unique identifiers, or web links for publicly available datasets
- A description of any restrictions on data availability
- For clinical datasets or third party data, please ensure that the statement adheres to our policy

The data supporting the findings of this study are provided within the paper and its supplementary information. The raw and analysed datasets generated during the study are available for research purposes from the corresponding authors on reasonable request.

Research involving human participants, their data, or biological material

Policy information about studies with human participants or human data. See also policy information about sex, gender (identity/presentation), and sexual orientation and race, ethnicity and racism.

Reporting on sex and gender	We imaged four males and four females
Reporting on race, ethnicity, or other socially relevant groupings	Race, ethnicity and other social groupings were not considered with regards to the analysis and conclusions of this study.
Population characteristics	All recruited participants were healthy.
Recruitment	Participants were recruited from the California Institute of Technology.
Ethics oversight	The study was approved by the Institutional Review Board of the California Institute of Technology.

Note that full information on the approval of the study protocol must also be provided in the manuscript.

Field-specific reporting

Please select the one below that is the best fit for your research. If you are not sure, read the appropriate sections before making your selection.

☒ Life sciences ☐ Behavioural & social sciences ☐ Ecological, evolutionary & environmental sciences

For a reference copy of the document with all sections, see nature.com/documents/nr-reporting-summary-flat.pdf

Life sciences study design

All studies must disclose on these points even when the disclosure is negative.

Sample size	The scope of this work was technology development. We recruited eight participants.
Data exclusions	No data were excluded from the study.
Replication	The reproducibility of the findings was evaluated via repeated measurements for each participant as well as in different anatomical regions across participants.
Randomization	The participants joining the study were randomly recruited.
Blinding	The investigators were blinded to group allocation during data collection and analysis.

Reporting for specific materials, systems and methods

We require information from authors about some types of materials, experimental systems and methods used in many studies. Here, indicate whether each material, system or method listed is relevant to your study. If you are not sure if a list item applies to your research, read the appropriate section before selecting a response.

Materials & experimental systems

n/a	Involved in the study
☒	☐ Antibodies
☒	☐ Eukaryotic cell lines
☒	☐ Palaeontology and archaeology
☒	☐ Animals and other organisms
☒	☐ Clinical data
☒	☐ Dual use research of concern
☒	☐ Plants

Methods

n/a	Involved in the study
☒	☐ ChIP-seq
☒	☐ Flow cytometry
☒	☐ MRI-based neuroimaging